Check for updates

View Article Online
View Journal

Journal of Materials Chemistry A

Materials for energy and sustainability

Accepted Manuscript

This article can be cited before page numbers have been issued, to do this please use: X. C. Zeng and Q. Liu, *J. Mater. Chem. A*, 2026, DOI: 10.1039/D6TA00037A.

This is an Accepted Manuscript, which has been through the Royal Society of Chemistry peer review process and has been accepted for publication.

Accepted Manuscripts are published online shortly after acceptance, before technical editing, formatting and proof reading. Using this free service, authors can make their results available to the community, in citable form, before we publish the edited article. We will replace this Accepted Manuscript with the edited and formatted Advance Article as soon as it is available.

You can find more information about Accepted Manuscripts in the Information for Authors.

Please note that technical editing may introduce minor changes to the text and/or graphics, which may alter content. The journal's standard Terms & Conditions and the Ethical guidelines still apply. In no event shall the Royal Society of Chemistry be held responsible for any errors or omissions in this Accepted Manuscript or any consequences arising from the use of any information it contains.

ROYAL SOCIETY OF CHEMISTRY

rsc.li/materials-a

View Article Online
DOI: 10.1039/D6TA00037A

ARTICLE

Open Access Article. Published on 16 March 2026. Downloaded on 3/17/2026 4:36:31 AM.
This article is licensed under a Creative Commons Attribution-NonCommercial 3.0 Unported Licence.

Journal of Materials Chemistry A Accepted Manuscript

Quasi-Low-Dimensional Perovskite with Enhanced Stability Against Lattice Strain and Desired Band Edge by A-Site Design†

Received 00th January 20xx,
Accepted 00th January 20xx

DOI: 10.1039/x0xx00000x

Qi Liu and Xiao Cheng Zeng*[a]

Abstract: Quasi-low-dimensional (QLD) additive engineering offers a compelling strategy for stabilizing layered perovskites against lattice strain (Hou et al., *Science*, **2025**, 387, 1069) while tuning the band-edge states. Another recent experiment also demonstrated that the incorporation of charged π-stacking aromatic conjugation (CPAC) A-site cations into the prevailing bulk perovskite for solar cells can lead to reduced bandgaps owing to the strong aromatic polarity of the CPAC cations (Zhu et al., *Nat. Commun*., **2024**, 15, 2753). In this work, by employing both QLD-additive and CPAC cation design strategies and density-functional theory computation, we examined four CPAC terminal spacers in QLD perovskites: Tropylium (Tr), Pyridinium (Py), N-Methylpyridinium (Mp), and N-Ethylpyridinium (Ep), and the hybrid frameworks of the QLD perovskite stacked with nMAPbI3 layers. Our calculation results show that Tr cation spacer, with the highest aromaticity among the four spacers, lead to the lowest conduction band minimum (CBM) once Tr-based QLD perovskite is stacked with a multilayer nMAPbI3 perovskite. Additionally, as the thickness (n) of multilayer nMAPbI3 increases, the CPAC spacers with stronger steric hindrance tend to induce phase segregation by lattice strain, leading to irregular band-gap-thickness gradients. Lattice strain resistance analysis indicates that both Tr and Py spacers, benefiting from their relatively strong hydrogen–halogen van der Waals interaction, offer relatively high tolerance to lattice deformation. These theoretical findings suggest that the integration of optimal CPAC spacers in QLD perovskites can be an effective design strategy to enhance structural stability against lattice strain while fine-tuning electronic structures for making durable optoelectronic devices.

1 Introduction

Perovskite solar cells (PSCs) have attracted considerable attention in the field of photovoltaics due to their remarkable characteristics, including high photovoltaic conversion efficiency (PCE), cost-effectiveness, and simple fabrication processes.[1–3] The first PSC, developed by Miyasaka et al., initially exhibited a modest PCE of 3.8%.[4] To date, on-going advancements have propelled the certified PCE of single-junction perovskite solar cells beyond 27.0%.[5] Despite notable advancements, several limitations remain for achieving efficient carrier mobility and high chemical stability, optimizing optical absorption across a broad spectral range, and establishing clear relationships between structure and PCE. Tackling these issues is crucial for further improvement of the performance of PSCs.

QLD Ruddlesden-Popper (R-P) layered perovskites have emerged as promising candidates for making solar cells due to their easy-to-realize chemical stability and versatile optoelectronic properties. Structurally, these QLD R-P perovskites consist of inorganic PbI_6^{4-} octahedral layers interspersed with large A-site cation spacers such as phenylethylammonium (PEA, $PhCH_2CH_2NH_3^+$) or butylammonium (BA, $CH_3(CH_2)_4NH_3^+$). The hydrophobic alkyl cations with relatively large spatial hindrance shield the perovskite framework from solvolysis in polar solvents while improving interface charge extraction and reducing surface defects, thereby mitigating degradation deficient that often occur in bulk inorganic-organic perovskites.[6–9] Moreover, the energy funneling effect, as demonstrated by Yang et al.,[10] can facilitate directional carrier migration due to the bandgap and work-function gradients (induced by the thickness gradient), thereby allowing optical absorption over broad wave-length range.[10 –19] Additionally, compared to their 3D counterparts, QLD R-P perovskites exhibit stronger defect resistance, owing to the A-site spacers, thereby achieving longer effective lifetime.[20,21]

However, QLD R-P perovskites still have limitations. The relatively large organic spacers tend to disrupt carrier transport due to the overall localized electronic states and narrowed band dispersions. The large spacers also introduce significant carrier-mobility anisotropy at heterointerfaces of hybrid perovskites, lowering overall device performance. To address these limitations, charged π-stacking aromatic conjugation (CPAC) has emerged as a promising strategy for designing effective spacers that can lead to suitable band structures for the QLD perovskites. A CPAC structure typically involves one or more charged aromatic rings, for example, protonated pyridines (Py^+, $C_5H_5NH^+$) or deprotonated cyclopentadienes (Cp^-, $C_5H_5^-$). Theoretically, density-functional theory (DFT) calculations have predicted that CPAC spacers like pyridiniums can yield enhanced electronic delocalization and a downshift of the conduction band minimum (CBM), thereby broadening the light absorption range.[22-28] These theoretical predictions have been confirmed by recent experiments. For example, Yu et al. showed that their air-fabrication perovskite cells

*a Department of Material Science and Engineering, City University of Hong Kong, Hong Kong SAR 999077, China. *Email: xzeng26@cityu.edu.hk*
† Electronic Supplementary Information available

View Article Online
DOI: 10.1039/D6TA00037A

Open Access Article. Published on 16 March 2026. Downloaded on 3/17/2026 4:36:31 AM.
This article is licensed under a Creative Commons Attribution-NonCommercial 3.0 Unported Licence.

Journal of Materials Chemistry A Accepted Manuscript

with ionic liquid containing pyridinium salt can yield a high PCE of 25.11%. Also, the moisture-resistance effect of pyridinium cations and their quaternary ammonium derivatives (or quats) have been confirmed by experiments.[29-33] A stronger CPAC-ring system can even give rise to higher PCE. Recently, Zhu et al.[34] designed a QLD perovskite ($MVPb_2I_6$) containing inter-molecular coupled "paraquat" CPAC cations, and showed that such a CPAC-based QLD perovskite can suppress interfacial non-radiative recombination and improve carrier extraction. Notably, $MVPb_2I_6$ can yield a high PCE of 25.66% with 95% efficiency retention over 1000 hours. Nelson et al.[35,36] successfully synthesized a series of 1D linear perovskite containing an aqua-solution stable CPAC carbocation, tropylium ($C_7H_7^+$, or *approx.* Tr^+ in this article) with linear MI_6 (M=Sn^{4+}, Pb^{2+}, Bi^{3+}, and Sb^{3+}) frameworks, and they achieved narrow-bandgap QLD perovskites with broadened absorption range in visible spectra.

Electronic structures in bulk perovskites are susceptible to external strains. Theoretical predictions indicate that a 5% lattice strain can induce marked band distortion, leading to a transition from a direct to an indirect bandgap.[37–42] Also, phase segregation frequently occurs spontaneously in mixed-composition perovskites under various strains. Such strain-induced phase segregation can generate various molecular intermediates, leading to structure defects such as grain boundaries.[43] QLD R-P perovskites, however, can exhibit stronger resistance to lattice strain compared with their 3D analogs.[44–46] Hou et al. reported that 2D perovskite coating can enhance lattice stability and suppress light-induced lattice expansion, a common issue in bulk perovskites.[47] Our previous theoretical studies have also shown that 2D coating can stabilize highly active phosphonium perovskite frameworks such as $MPSnBr_3$.[48] Note that while bulky organic cations contribute to structural stability, they tend to incur highly localized bands near the Fermi level and restrict charge carrier migration. As a result, QLD perovskite-based solar cells often exhibit lower PCE than their 3D counterparts.[16] To mitigate these limitations, terminal spacers with good strain-resilience and suitable bandgap are required for the design of more efficient and stable QLD perovskites.

In this work, we systematically investigated a series of layered QLD perovskites, namely, $A_2PbI_4 \bullet nMAPbI_3$, with incorporating various CPAC A-site spacers, including protonated pyridine (Py, $C_5H_5NH^+$), N-methylpyridinium (Mp, $C_5H_5N{-}CH_3^+$), N-ethylpyridinium (Ep, $C_5H_5N{-}C_2H_5^+$), and tropylium (Tr, $C_7H_7^+$). Here, the number of $MAPbI_3$ filling layers (*n*) was varied from 0 to 4. Density-functional theory (DFT) calculations were employed to predict the geometric and electronic structures of these QLD perovskites. Our results show that bulky CPAC spacers can introduce strong steric effects that result in rearrangement of the PbI_6^{4-} octahedral framework with increasing layer number (*n*). Such steric effects could trigger phase segregation and yield irregular band-gap-thickness relations, contrary to non-CPAC spacers such as PEA and BA. Furthermore, structural responses to externally applied strain were examined, highlighting distinct deformation behaviors modulated by the CPAC spacers. The overarching aim of this study is to elucidate how CPAC-induced structural perturbation modifies the overall electronic properties and enhances strain resistance of QLD perovskites. By establishing a mechanistic understanding and by proposing a representative model sequence of CPAC-based perovskites, this work provides a groundwork for future experimental validation and potential utilization of these newly predicted materials in high mobility or high strain-resilient optoelectronic devices.

2 Computational Methods

First-principles DFT calculations were performed with the Vienna Ab Initio Simulation Package (VASP 6.4)[49–51] to compute the geometric, electronic structures of all the bulk and QLD perovskites considered in this work, as well as their heterojunction with a charge transfer layer. The projector augmented wave (PAW) pseudopotentials with the cutoff energy of 600 eV were employed. The generalized gradient approximation (GGA) exchange-correlation functional, Perdew-Burke-Ernzerhof (PBE), with the DFT-D3 dispersion correction method of Grimme with zero-damping[52–54] were applied to optimize the geometrical structures. During the structural optimization, all atoms were allowed to relax until every atom was in mechanical equilibrium without any residual force > 10^{-4} eV/Å.

To compute the electronic structures of the perovskites, the more accurate HSE06 functional was used as it includes a fraction of screened Hartree-Fock (HF) exchange to improve the discontinuity associated with the derivative of the Kohn-Sham potential at integer electron numbers. Here, the HF exchange parameter α = 0.38 was chosen so that our DFT calculation results can be closer to the experimental data. For the non-CPAC benchmark, PEA, the default HF exchange parameter α = 0.2 was kept. Additionally, the spin-orbit coupling (SOC) effect was accounted for (due to the presence of the heavy atom Pb in the perovskites) in all DFT calculations except geometrical optimization. More specifically, we calculated the partial density of states (pDOS) and optical absorption data of $MV[PbI_3]_2$[24] at the HSE06+SOC level of theory to reproduce the experimentally measured band-gap width (see ESI Figure S1). The electronic constituents were 6s 5d 6p for Pb; 5p 6s for I, 5p 6s 4f for Cs, 2s 2p for C, N, and 1s for H. For all the calculations on QLD perovskite slab systems, a 25Å vacuum layer was adopt so that the spurious interaction among z-direction periodic images would be negligible. All the QLD perovskite slabs were confirmed neutral; and the isolated spacer salts were calculated with its counter ions (I^-), as its relevant form in experimental conditions. To further reduce any residual periodic-image effects associated with the organic spacers, a 2 × 2 supercell was used for property calculations. Also, for all the QLD systems, we adopted the Monkhost-Pack scheme of 4×4×1 gamma-centered *k*-point grid for self-consistent calculation. For computing the band structures, we generated the linear sequences of high-symmetrical points (20 *k-points* per range) within every lattice vector.

Aromaticity of the spacers was assessed by calculating nucleus-independent chemical shifts (NICS) values[55-57]. NICS calculations were carried out by using ORCA 6.1.1 package[58-63] at the B3LYP[64] level of theory along with the Gauge-including Atomic Orbital(GIAO)[65] method. The def2-TZVP basis[66] set was employed for all atoms. Specifically, NICS values of NICS(1), defined at 1.0 Å above the ring center along the ring normal, were calculated, using geometries extracted from the optimized spacer salts.

3 Results and Discussion

3-1 Structural and Stability of LD CPAC-based A_2PbI_4 Perovskite

We considered four CPAC spacers, including pyridiniums—protonated pyridine(Py), N-methylpyridium(Mp), and N-ethylpyridinium (Ep), as well as a stable carbocation-bearing species, tropylium (Tr).[25,26] The conventional non-CPAC terminal cation, phenylethylammonium (PEA), was also considered as a benchmark for comparison. The optimized geometric data of all spacers are shown in Figure S2. The Mp and Ep cation shares a similar geometric

This journal is © The Royal Society of Chemistry 20xx

Please do not adjust margins

View Article Online
DOI: 10.1039/D6TA00788C

structure as PEA, but its nitrogen atom with a positive charge is integrated into the aromatic ring (analogous to Py[21,23,40] and MV[24]), leading to a polarized aromatic ring structure with nonuniform charge delocalization. In contrast, the Tr cation exhibits uniform charge delocalization across its seven-carbon tropylium ring (similar to the cyclopentadienyl anion), endowing it with exceptional charge transfer capability.

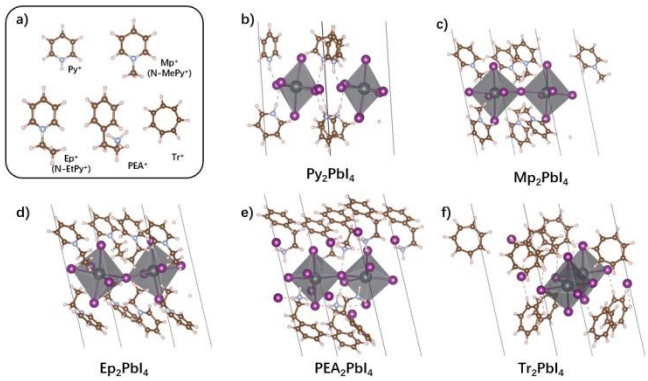

Figure 1. (a) Optimized spacer cations (CPAC and PEA for benchmark) and (b-f) low-dimension perovskite with various spacers. The optimized supercells are shown in Figure S3.

The optimized spacer cations and LD perovskite layers—Py_2PbI_4, Mp_2PbI_4, Ep_2PbI_4, Tr_2PbI_4, and PEA_2PbI_4 (for benchmark) — are shown in Figure 1. These QLD perovskites possess elongated PbI_6^{4-} octahedra along the *z*-axis, which are induced by the insertion of the bulky CPAC spacers. As shown in Table 1, in general, the structure of A_2PbI_4 perovskites highly depends on the molecular geometry of the A-site cations. Flat pancake-like spacers such as pyridinium (Py) and tropylium (Tr) with large Φ_A(diameter) values, tend to form linear, face-sharing 1D structures.[25,40] In contrast, Ep, Mp, and PEA spacers can stabilize 2D arrangements with two face-sharing and one vertex-sharing Pb-I layers due to their polar characteristic and small steric side chain that can be inserted into the PbI_6^{4-} frameworks.

Table 1. Optimized low dimensional (1D/2D) CPAC perovskites A_2PbI_4 and computed formation energies. Here, the bracketed A-I length represents the minimum distance between I^- and the H^+(proton) donor in the functional group, e.g. H in $-NH_3^+$

Spacers	Py	Mp	Ep	PEA	Tr
Φ_A	2.73	4.23	4.99	5.15	3.26
a	7.55	9.61	8.98	7.80	8.78
b	10.14	10.18	10.17	9.51	10.58
h	12.27	13.28	12.84	16.11	10.89
α	77.89	78.94	77.86	81.56	104.63
β	90.85	94.78	97.41	90.80	81.39
max d_{Pb-I}/Å	3.38	3.39	3.36	3.32	3.32
avr. d_{Pb-I}/Å	3.21	3.28	3.26	3.26	3.25
I-Pb-I /deg.	81.6	82.46	87.56	82.83	81.89
d_{A-I} /Å	3.37(2.47)	3.98	4.09	3.38(2.40)	4.66(2.91)
E_{form}/ meV/atom	-139.27	-28.35	-77.47	-117.47	-90.04

Intermolecular interactions can further differentiate these QLD perovskite systems in terms of the influence of the A-site cation spacer on the stability against lattice strain and the band edge state. Since Py and PEA possess polarized N–H bonds that can have close van der Waals contact with surface iodides (2.40–2.47 Å), more negative formation energies are resulted, indicating stronger binding between surface iodide and the H^+ donor. Although Tr lacks high-electronegativity H^+ donor (like $-NH_3^+$ or $=N^+H$-), its π-delocalized charge distributes upon all the ring carbons, enabling weaker but still stable van der Waals contact (2.91 Å; E_{form} = −90.04 meV) that can provide modest resistance to lattice strain. In contrast, the quaternized pyridinium cations (Ep and Mp) lack H^+ donors, and they interact primarily with terminal iodides via Coulombic attraction, resulting in relatively longer vertical Pb–I distances (3.36–3.39 Å) and less negative formation energies. In particular, Mp (E_{form} = −28.35 meV/atom) results in less stability due to the short alkyl substituent. The latter allows deeper pyridine insertion that can disrupt Pb–I bonding. Such structural distortions can also localize hole states near the valence band maximum (VBM), likely reducing carrier mobility. In Figure 2, the computed electronic structures, including the bandgaps at different levels of theory, effective carrier masses, and optical absorption spectra, are shown. The detailed pDOSs are shown in Figure S4. As shown in Figure 2a, all CPAC-based QLD perovskites exhibit reduced bandgaps, compared to the ring-uncharged PEA-based structure (benchmark), thereby enhancing visible light absorption and facilitating charge transfer. Among the pyridinium-based cation species (Py, Mp, Ep), the bandgap decreases as the N-alkyl chain length increases. Notably, Tr-based perovskite has the narrowest bandgap due to the extended conjugation across seven carbon atoms, effectively lowering the CB edge.

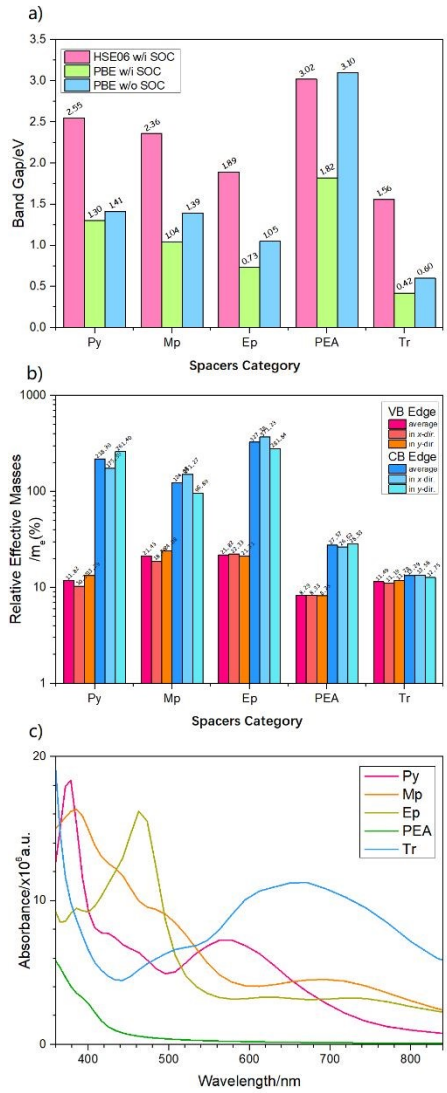

Figure 2. Computed (a) bandgaps, (b) effective carrier masses, and (c) optical absorption spectra of CPAC-based LD perovskite A_2PbI_4 with different

Open Access Article. Published on 16 March 2026. Downloaded on 3/17/2026 4:36:31 AM.
This article is licensed under a Creative Commons Attribution-NonCommercial 3.0 Unported Licence.

Journal of Materials Chemistry A Accepted Manuscript

Please do not adjust margins

View Article Online
DOI: 10.1039/D6TA00371A

Open Access Article. Published on 16 March 2026. Downloaded on 3/17/2026 4:36:31 AM.
This article is licensed under a Creative Commons Attribution-NonCommercial 3.0 Unported Licence.

terminal spacers and different levels of theory Here, "w/i" denotes an abbreviation for "within", and "w/o" for "without".

It is known that carrier transport is strongly dependent on carrier's effective mass.[67–71] The effective masses of carriers for the CPAC-based LD perovskites were determined by fitting the energy dispersions of the VB and CB edges to quadratic functions, i.e., $\frac{1}{m_{ii}^*} = \frac{1}{\hbar}\frac{\partial^2 E_n(\kappa_i)}{\partial \kappa_i^2} (i = x,y)$, where m_{xx} and m_{yy} correspond to the effective mass along the *x* and *y* directions, respectively, and E_n represents the computed band dispersions at the given *k*-point vector (see Figure S5). Figure 2b illustrates that all CPAC-based QLD perovskites exhibit higher electron effective masses (m^*) than the corresponding bulk perovskite (benchmark; $0.06m_e$) due to reduced dimensionality. Quat pyridinium-based structures (Mp, Ep) exhibit abnormally large m^* values (> $2m_e$) at the CBM, indicating strong carrier localization with hindered carrier transport, consistent with prediction based on the electronic structures. The effective-mass anisotropy in *x* and *y* directions further suggests slower carrier transport along the *y*-orientation, limiting overall mobility. Figure 2c shows the computed optical absorption spectra, where all CPAC-based structures display enhanced absorption in the visible range, compared with PEA_2PbI_4. Especially, Tr_2PbI_4's spectrum extends into the near-infrared region, owing to its narrowed bandgap. The observed redshift in absorption peaks is highly correlated with relatively large pyridinium alkyl length, as well as consistent with the trend predicted based on the bandgaps. Thus, the incorporation of CPAC spacers introduces delocalized CBM states that can improve light harvesting through tunable band edge, thereby addressing inherent optical limitations of QLD perovskites

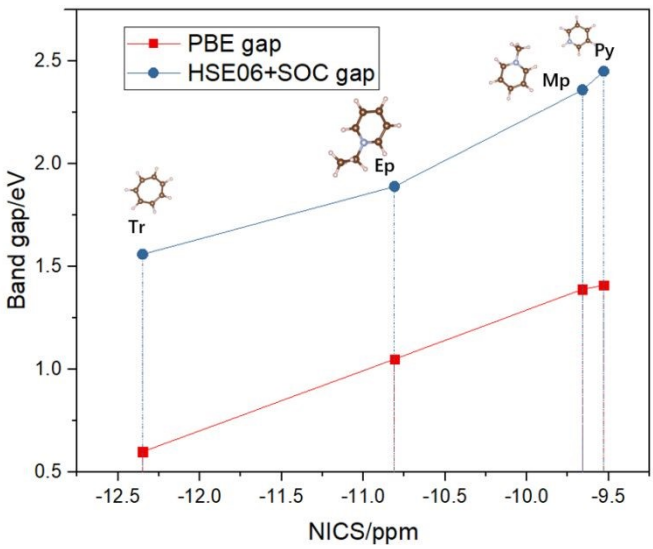

Figure 3. Calculated band gaps of the LD perovskite layers versus NICS (as NICS(1)) of their spacers.

To further clarify the relationship between spacer aromaticity and the electronic structure of LD perovskites, we calculated the NICS[55-57] (as NICS(1)) values of the aromatic spacers considered, and compared these values with the computed band gaps shown in Figure 2. As shown in Figure 3, the band gaps of CPAC-terminated QLD perovskites exhibit an approximately linear correlation with the NICS values of the corresponding terminal cations. It is worth noting that, although PEA shows a relatively low NICS value (~ −10.3), its band gap is markedly wider than those of CPAC-terminated LD perovskite structures because the positive charge center in PEA does not participate in the extended π-conjugation. These results further support our conclusion that CPAC cations make an effective contribution to the electronic states near the Fermi level in LD perovskites, and that stronger aromatic conjugation enables deliberate and quantitative tuning of the band gap.

3-2 Structural and Stability of QLD CPAC-based A_2PbI_4 Perovskite

Next, we theoretically designed QLD R-P perovskite frameworks, aiming to achieve structural flexibility through controlled variation of the layer thickness. The PEA structures were excluded from further consideration, as they do not offer the CPAC effect at their charged ammonium termini. To describe the ordering of PbI_6^{4-} octahedra within the newly designed frameworks, we adopted two abbreviations: (1) "F" denotes face-sharing, and (2) "V" denotes vertex-sharing connectivity. For instance, a 2F-1V sequence indicates a structural motif with two face-sharing octahedra and one vertex-sharing unit. As illustrated in Figure S6, CPAC-based frameworks with two $MAPbI_3$ layers exhibit cross-linked 2F–1V motifs capped by quasi-linear 1D coatings, reflecting the structural constraints imposed by the bulky spacers. In contrast, the frameworks with three or more stacked layers display parallel 2F-1V sequences, including the terminal layers with spacers. These structural configurations resemble those observed in standard quasi-2D $MAPbI_3$ layered perovskites.

To assess the structural stability of these hybrid layer-stacked frameworks, particularly those involving large spacers, we evaluated their phase-segregation tendencies by computing the reaction energy associated with a net decomposition reaction:

$$A_2PbI_4 \cdot nMAPbI_3 \rightarrow A_2PbI_4 + (MAPbI_3)_n \quad (1)$$

where the phase-segregation energy is defined as $E_{seg} = E_{QLD} - (E_{A_2PbI_4} + E_{(MAPbI_3)_n})$ and *n* represents the thickness of the $MAPbI_3$ layers. The phase-segregation energy is a measure of the thermodynamic favorability toward surface-layer dissociation, especially in multi-layered structures. It also reflects the limits of structural resilience of CPAC-based layered perovskite frameworks: $A_2PbI_4 \cdot nMAPbI_3$. The calculated largest Pb-I distance at the surface and segregation energies of various frameworks with different CPAC spacers and *n* are summarized in Figure 4, and the detailed geometric parameters are given in Tables S1 and S2. As shown in Figure 4a, extended Pb–I bond length reflects weak coupling between CPAC spacers and the inorganic framework, suggesting a tendency for CPAC spacers to detach from the surface by releasing A^+ and I^- ion pairs. An exception is the smallest CPAC spacer, Py, whose H^+ donor is engaged in stronger van der Waals interaction with the PbI_6^{4-} octahedra, which helps to stabilize the surface. The Tr cation also contains H^+ donor, but its uniform electron delocalization lowers the overall polarity, weakening the van der Waals interaction while slightly increasing the Pb–I bond length.

The phase segregation is more likely to occur in the case of quat cations such as Mp and Ep due to the absence of H^+ donor and hydrogen bonding (see Figure 1, Figure S3 and S6). Additionally, the

Journal of Materials Chemistry A Accepted Manuscript

This journal is © The Royal Society of Chemistry 20xx

Please do not adjust margins

View Article Online
DOI: 10.1039/D5TA09...

bulky size of the quat cations and their strong electrostatic interaction can further distort the PbI_2-terminated surface structure. Especially $Ep_2PbI_4 \cdot n$,$MAPbI_3$ ($n > 3$) show considerable detachment of isolated EpI and $MAPbI_3$ species due to Ep's large size with the longest maximum Pb-I distance up to 6 Å, among all cations considered.

As depicted in Figure 4b and Table S4, the phase-segregation energies increase sharply when CPAC-based QLD perovskite layers form heterojunction with $MAPbI_3$, particularly in Py_2PbI_4 and Tr_2PbI_4, where H^+ donor alters the octahedral connectivity at terminal interfaces. With increasing $MAPbI_3$ thickness (n), the segregation energies gradually decrease, indicating higher thermodynamic favorability for phase segregation. This trend reflects both the diminished impact of van der Waals interaction on the stability, and the growing mismatch between the QLD spacer surface and the $MAPbI_3$ interlayers. Notably, for $n > 3$, segregation energies converge across all CPAC-based frameworks, suggesting that beyond $n = 3$, the CPAC-based QLD perovskite structures approach a bulk-like $MAPbI_3$ structure. The interfacial mismatch between the CPAC-based QLD perovskite structure and $MAPbI_3$ enhances the likelihood of phase segregation toward separated A_2PbI_4 and $MAPbI_3$ domains. Given the reduced structural influence of CPAC spacers beyond n =3, we will not consider strain-induced electronic effects for $n > 3$.

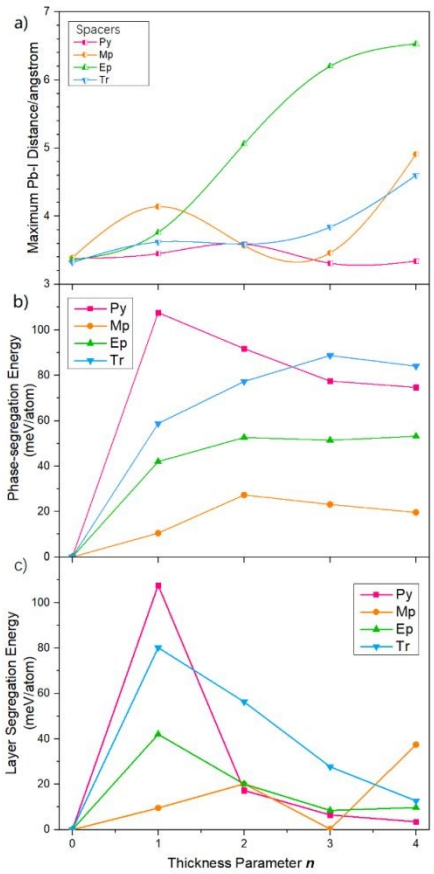

Figure 4. Computed (a) maximum Pb-I distance at the surface, (b) phase-segregation energy and (c) layer-segregation energy of CPAC-based layered perovskite frameworks (A_2PbI_4 • nMAPbI$_3$) with different spacers versus $MAPbI_3$ layer thickness n.

Figure 4c and Table S5 display the calculated layer segregation energy, which represents the opposite of the interlayer binding energy as:

$$A_2PbI_4 \cdot nMAPbI_3 \rightarrow A_2PbI_4 \cdot (n\text{-}1)MAPbI_3 + MAPbI_3 \ (n = 1 \text{ to } 4) \quad (2)$$

Among the QLD perovskite structures, the Py cation exhibits the strongest ability to suppress layer segregation. However, since only the N–H group can form hydrogen bonds (bond length: 2.41 Å), its stabilization effect *via* hydrogen bonding imposes certain constraints on the arrangement and orientation of the lead iodide octahedra. As the number of perovskite layers increases, the hydrogen-bonding stabilization is partially suppressed due to the reorientation of the pyridine nitrogen.

In contrast, the Tr cation features uniform π-delocalization, rendering all seven hydrogens on its ring equivalent and capable of forming hydrogen bonds. Consequently, it behaves more uniformly with increasing perovskite layer count, a trend that stands in clear contrast to the Py-capped perovskites. Furthermore, since the hydrogen bonds formed by Tr are weaker (bond length: 2.91 Å), the maximum layer segregation energy of Tr-capped perovskites is lower than that of Py-capped ones. Owing to the absence of polar hydrogen atoms, Mp and Ep cations generally exhibit lower resistance to layer segregation.

The overall structural modifications, including elongated Pb–I distance, surface polarization, and interface mismatch, can alter the electronic structure of QLD perovskites. Variations in CPAC terminal species and layer thickness (n) can result in systematic bandgap shifts and different optical responses, underscoring a tight coupling between interfacial structure and electronic behavior of these hybrid frameworks. The calculated n-dependent bandgaps are presented in Figure 5, and orbital-level insights provided by pDOS are shown in Figures S7–S10.

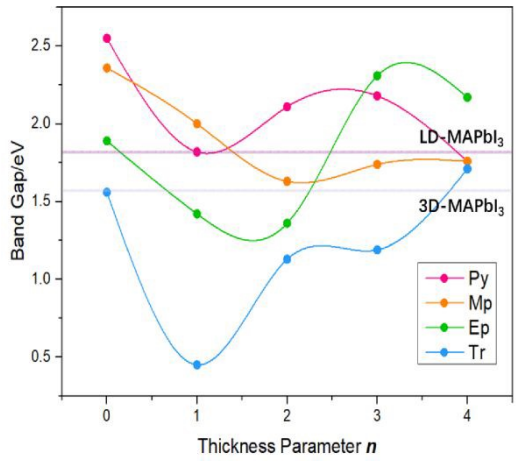

Figure 5. Computed bandgaps of multilayer R-P CPAC-based perovskite A_2PbI_4 • nMAPbI$_3$ with different spacers, at the HSE06+SOC level of theory. The horizontal purple lines show the 3D- and QLD-structure of pure $MAPbI_3$ for comparison.

The pDOS indicates that CPAC-based QLD perovskites are still dependent on n. However, due to the low CB edge and strong steric hindrance of CPAC spacers, the pDOS dependence of n deviates markedly from the linear trend typical of PEA or BA based systems.[10,14,16–18,72] As illustrated in Figure 4, the bandgap initially decreases as n increases from 0 to 1, regardless of the structure of spacers. This band-gap reduction can be attributed to the enhanced connectivity within the $[PbI_6]^{4-}$ octahedral framework, facilitated by the cross-linking effect of $MAPbI_3$. For CPAC spacers with H^+ donor such as Py and Tr, the substantial lattice mismatch between the flat spacers and the 3D $[PbI_6]^{4-}$ framework results in a large reduction of bandgap from n = 0 to n = 1. The calculated band structures (see Figure S11) confirmed this result. This is primarily due to steric incompatibility that weakens the internal Pb-I interaction and

Open Access Article. Published on 16 March 2026. Downloaded on 3/17/2026 4:36:31 AM.
This article is licensed under a Creative Commons Attribution-NonCommercial 3.0 Unported Licence.

Journal of Materials Chemistry A Accepted Manuscript

Please do not adjust margins

Open Access Article. Published on 16 March 2026. Downloaded on 3/17/2026 4:36:31 AM.
This article is licensed under a Creative Commons Attribution-NonCommercial 3.0 Unported Licence.

elevates the VB edge. For Tr-based structures, the stronger CPAC effect further downshifts the CB edge to a minimum of 0.84 eV, thereby enhancing optical absorption capability towards visible and near-infrared regions.

For quat spacers such as Mp and Ep, the absence of H^+ donors together with their significant steric hindrance lead to enlarged spatial separation between the positively charged centers and neighboring iodide ions in CPAC-based QLD perovskites, particularly for n = 1–2. Beyond n = 2 , the bandgap of the CPAC-based QLD perovskites starts to increase gradually with n and eventually converges to an asymptotic value, a characteristic of layered $MAPbI_3$ with a 2F-1V octahedral stacking sequence (see Figure S12), independent of the CPAC type. This convergence suggests that the inductive and steric effects of CPACs on the $[PbI_6]^{4-}$ framework become diminished for n > 3. Among the cations considered, Ep is the most destabilizing one since its large steric demand tends to promote strong phase segregation for n > 3, as reflected by the reduced cross-linked structures of the Pb–I network and increased bandgaps. These results confirm that the CPAC spacers are very effective for engineering band edges of multilayer heterostructures (n < 3), where their steric and electronic interactions remain strongly coupled with the PbI_6^{4-} framework. Beyond n = 3, their influence diminishes, and the electronic structure becomes increasingly dictated by the bulk $MAPbI_3$ properties.

3-3 How do CPAC-based QLD Perovskites with H^+ Donor Show Good Strain Resilience

QLD layered perovskites are often subjected to spontaneous strain tension under various external conditions[45-47]. To further understand this behavior, the strain response of CPAC-based QLD perovskites under different degrees of biaxial strain were investigated. As aforementioned, for structures with n ≥ 3, the influence of terminal CPAC spacers becomes minimal. Thus, in this section, we only focused on QLD configurations with n = 0 - 2. The calculated deformation energies and the maximum surface Pb-I bond length under various biaxial strains (-5%, -2% as compression, and +2%, +5% as extension) are shown in Figure 5, while more detailed data are shown in Tables S6 and S7. Here, the strain is given by:

$$\epsilon_{deform.} = \frac{E_{strain} - E_{pristine}}{N} \quad (3)$$

Where ϵ_{deform} represents the deformation energy, E_{strain} is the energy of a layered QLD structure under biaxial strain, $E_{pristine}$ represents the energy without strain (see Table 1 and Table S7), and N represents the thickness of the $MAPbI_3$ stacked layers. In the QLD perovskite structures, spacers such as Tr and Py have the highest resistance to deformation due to their tensed 1D-linear connectivity. The deformation energy of Py was found to be higher than that of Tr, attributed to the polarity of the Py cation. Specifically, the iodide anion interaction—arising from van der Waals forces between the polar hydrogen of Py and the perovskite surface—shows a shorter H–I distance (2.58 Å) compared to Tr (2.91 Å).

Furthermore, in the case of a single $MAPbI_3$ layer (n = 1), an intermediate conformation forms between the 1D linear Py/Tr_2PbI_4 and the 3D cross-linked cubic lattices. This intermediate structure weakens the Pb–I interactions, increases the structural distortion, and ultimately results in a lower deformation energy. This observation aligns with previous discussion without strain-induced deformation. Nevertheless, for the hybrid perovskite structure of QLD $A_2PbI_4 \cdot nMAPbI_3$, the slightly thicker n = 2 structure still exhibits lower strain tolerance than the rigid monolayer structure (n = 0), despite possessing a higher deformation energy than the well-characterized reference pure-phase perovskite (e.g., $[FACs]_{0.5}PbI_3$ in Figure S15)[47], except in the cases of large strain of +5%. The monolayer perovskite Tr_2PbI_4 shows a strong deformation tendency toward phase segregation under compressive strain (see Figure 6(b) and Tables S6 to S7) due to its relatively large and flat size with low polarity, which gives rise to a large deformation energy (Figure 6a). However, the nMAPbI$_3$-layer (n ≥ 1) stacked QLD structures kept the 3D linkage among various layers with the orientation change of the spacers (see Figures S13 - S16).

Due to the absence of H^+ donors, quat spacers such as Mp and Ep lack van der Waals interaction generated by the H^+ donor and $[PbI_6]^{4-}$ frameworks. As a result, the structures of n = 0 have fragile 2D planes with lower deformation energies. Incorporating $MAPbI_3$ stacked layers can enhance strain resistance through increased van der Waals coupling between MA cations and $[PbI_6]^{4-}$ framework. Moreover, as presented in Figure 6(b) and Table S7, structures that include Ep and Mp spacers show a pronounced increase in surface Pb–I distance ($d_{(Pb-I)}$) under compression, indicating structural instability and a higher tendency for phase segregation.

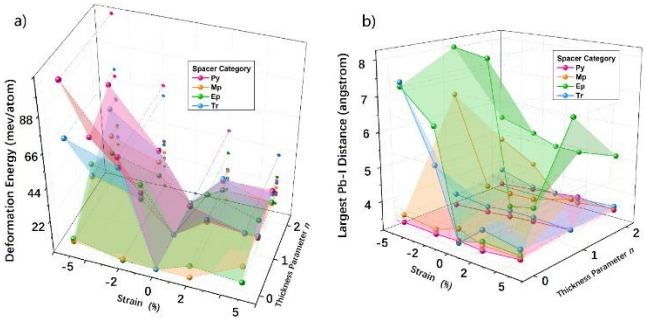

Figure 6. Computed (a) deformation energy (in meV/atom) and (b) the longest surface Pb-I distance (max. d_{Pb-I}) in multilayer CPAC-based perovskite $A_2PbI_4 \bullet nMAPbI_3$ (n = 0 to 2) with different spacers at various strains. Detailed numerical data are given in Tables S6 to S7. The data of $(FACs)_{0.5}PbI_3$ can be used as a comparative reference (see Figure S17).

We also investigated the strain-induced electronic responses for the QLD perovskites with various spacers. The calculated bandgaps are summarized in Figure 7, while detailed numerical values of the bandgaps and electronic density of states at various strains are given in Table S8 and Figures S18–S21, respectively. For perovskites terminated with spacers containing H^+ donor (Py and Tr), the bandgap shows systematic increases under tensile strain and decreases under compressive strain. This trend is consistent with that predicted based on the geometric deformation of the PbI_6^{4-} octahedral framework, with its structural coherence being largely maintained until phase segregation would occur. For instance, Py-based structures with n = 0 display a trend of bandgap increase from 1.99 eV at −5% to 2.54 eV at +5% strains, while Tr-based analogues display a trend of bandgap increase from 1.21 eV to 1.69 eV across the same range of strains.

Journal of Materials Chemistry A Accepted Manuscript

This journal is © The Royal Society of Chemistry 20xx

Please do not adjust margins

Open Access Article. Published on 16 March 2026. Downloaded on 3/17/2026 4:36:31 AM.
This article is licensed under a Creative Commons Attribution-NonCommercial 3.0 Unported Licence.

Journal of Materials Chemistry A Accepted Manuscript

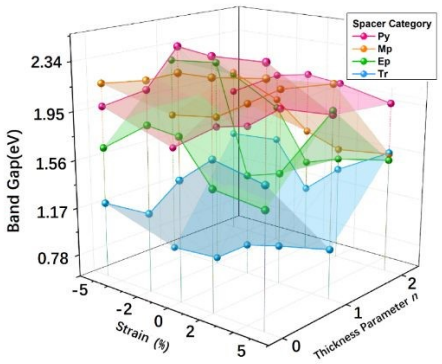

Figure 7. Computed bandgaps of multilayer R-P CPAC-based perovskites: A_2PbI_4 • nMAPbI$_3$ (n = 0 - 2) with different spacers and at various strains. DFT computation is at the theory level of HSE06+SOC. Detailed numerical data are given in Table S8.

By contrast, structures terminated with quat spacers (Mp and Ep) demonstrate a notably different response due to the absence of van der Waals interactions between the quat cations and the PbI_6^{4-} framework. At n = 0, their bandgaps remain relatively wide (e.g., 2.17–2.43 eV for Mp) —or behave irregularly under strain, reflecting partial segregation within the isolated spacer salts (MPI/EPI) and $[PbI_6]^{4-}$ networks. These structures display limited strain tolerance and are prone to phase segregation, particularly under compressive strains. The phase segregation, if it occurred, would lead to the formation of Q2D MAPbI$_3$ cubic layers with limited contribution from the terminal CPAC spacers. Consequently, a sharp increased bandgap is resulted, indicating the disruption of electronic coupling with respect to the strain-free structures and the reduced dimensionality of the perovskite framework. Overall, a consistent trend, across all spacer types, is that the n = 1 perovskite frameworks have the smallest bandgaps, irrespective of the external strain. This result suggests that the structures with modest thickness can retain optimal orbital overlap and lattice flexibility under mechanical perturbation, rendering them particularly favorable in tuning the bandgap for strain-engineering applications.

4 Conclusions

The nature of organic A-site cations plays a critical role in determining the optoelectronic characteristics of layered perovskites. The present study demonstrates that the organic CPAC spacers can have profound influence on the optoelectronic properties of QLD layered perovskites to evaluate how variations in terminal cation chemistry influence band gap behaviour, carrier effective mass, and optical absorption performance.

Our results demonstrate that the incorporation of charged aromatic rings significantly reduces the conduction band minimum (CBM), thereby narrowing the intrinsic wide band gap of conventional LD perovskites. This reduction follows the trend Tr > Ep > Mp > Py > PEA (as non-CPAC benchmark), correlating with the degree of delocalization in the charged aromatic heterocycles (inferred from NICS values). Notably, tropylium-terminated structures exhibit band gaps even lower than bulk MAPbI$_3$, expanding photo response into the visible and near-infrared regions—an advantageous trait for light-harvesting applications.

Regarding structural standpoint, the layered configurations show different tendencies to form QLD layered structures with MAPbI$_3$ layers. Although all QLD CPAC-based perovskites tend to phase segregate at thicknesses beyond n = 3 and release isolated spacer salts (PyI, TrI, MpI and EpI), this tendency can be suppressed by the van der Waals interaction provided by H^+ donor. In particular, Py and Tr spacers demonstrate enhanced interlayer cohesion due to van der Waals interaction with iodide anions, thereby suppressing the tendency of phase segregation while keeping structural integrity. In contrast, quat spacers, e.g., Mp and Ep which lack H^+ donors and have a large steric mismatch with the PbI_6^{4-} framework, tend to promote phase/layer segregation, thereby being less suitable for stable multilayer assembly.

The mechanical-strain response further highlights these distinctions. Py and Tr cations, due to their dipole moments and van der Waals interactions, exhibit superior tolerance to compressive strain. However, Tr's larger molecular diameter leads to compression-induced instability in monolayer configurations. On the other hand, quat cations Mp and Ep, dominated by electrostatic rather than dispersive interactions, show a strong propensity for phase separation under compression, as indicated by abrupt band gap shifts and low separation energies. Nonetheless, these QLD structures demonstrate notably high tolerance to tensile strain, offering potential utility for applications in mechanical deformation or lattice mismatch engineering.

The molecular-level insights gained from this study of substituting CPAC spacers in QLD perovskites will benefit future design of perovskite-based devices with structure flexible and light-harvesting features, as well as anisotropic charge transport potential, and tunable mechanical resilience.

Author contributions

Q. Liu designed and operated the DFT computational research and wrote the article. X. C. Zeng supervised the project. All the authors have been reviewed the article file.

Conflicts of interest

There are no conflicts to declare.

Data availability

A data availability statement (DAS) is required to be submitted alongside all articles. Please read our full guidance on data availability statements for more details and examples of suitable statements you can use.

Acknowledgements

X.C.Z acknowledges the support by Hong Kong Global STEM Professorship Scheme and the Research Grants Council of Hong Kong Grant (C1055-23G and CRS Cityu 104/24).

Notes and references

‡ Footnotes relating to the main text should appear here. These might include comments relevant not central to the matter under

View Article Online
DOI: 10.1039/D5TA00037A

discussion, limited experimental and spectral data, and crystallographic data.
§
§§
etc.

1 Jena, A.; Kulkarni, A.; Miyasaka, T. Halide Perovskite Photovoltaics: Background, Status, and Future Prospects. *Chem. Rev.* 2019, ***119***, 3036–3103.
2 Stranks, S. D.; Snaith, H. J. Metal-Halide Perovskites for Photovoltaic and Light-Emitting Devices. *Nat. Nanotechnol.* 2015, ***10***, 391–402.
3 Grätzel, M. The Light and Shade of Perovskite Solar Cells. *Nat. Mater.* 2014, ***13***, 838–842.
4 Kojima, A.; Teshima, K.; Shirai, Y.; Miyasaka, T. Light Sensitizers for Photovoltaic Cells. *J. Am. Chem. Soc.* 2009, ***131***, 6050–6051.
5 National Renewable Energy Laboratory (2025) Best Research-Cell Efficiencies. Available at https://www.nrel.gov/pv/cell-efficiency. 2025.
6 Ouyang, R. Exploiting Ionic Radii for Rational Design of Halide Perovskites. *Chem. Mater.* 2020, ***32***, 595–604.
7 Chakrabarti, T.; Kaarthik, S.; Perumal, A. Phenethylammonium Halide Blend as an Efficient Interlayer in Solution-Processed Inverted Planar p–i–n Perovskite Solar Cells. *ACS Applied Energy Materials* 2025, ***8***, 2837–2844.
8 Thrithamarassery Gangadharan, D.; Ma, D. Searching for stability at lower dimensions: current trends and future prospects of layered perovskite solar cells. *Energy Environ. Sci.* 2019, ***12***, 2860–2889.
9 Li, X.; Fu, Y.; Pedesseau, L.; Guo, P.; Cuthriell, S.; Hadar, I.; Even, J.; Katan, C.; Stoumpos, C. C.; Schaller, R. D.; Harel, E.; Kanatzidis, M. G. Negative Pressure Engineering with Large Cage Cations in 2D Halide Perovskites Causes Lattice Softening. *J. Am. Chem. Soc.* 2020, ***142***, 11486–11496.
10 Oddo, A. M.; Gao, M.; Weinberg, D.; Jin, J.; Folgueras, M. C.; Song, C.; Ophus, C.; Mani, T.; Rabani, E.; Yang, P. Energy Funneling in a Noninteger Two-Dimensional Perovskite. *Nano Lett.* 2023, ***23***, 11469–11476.
11 Quan, L. N.; Yuan, M.; Comin, R.; Voznyy, O.; Beauregard, E. M.; Hoogland, S.; Buin, A.; Kirmani, A. R.; Zhao, K.; Amassian, A.; Kim, D. H.; Sargent, E. H. Ligand-Stabilized Reduced-Dimensionality Perovskites. *J. Am. Chem. Soc.* 2016, ***138,*** 2649– 2655.
12 Yuan, M.; Quan, L.; Comin, R. e. a. Perovskite energy funnels for efficient light-emitting diodes. *Nature Nanotech.* 2016, ***11***, 872–877.
13 Liu, J.; Leng, J.; Wu, K.; Zhang, J.; Jin, S. Observation of Internal Photoinduced Electron and Hole Separation in Hybrid Two-Dimentional Perovskite Films. *J. Am. Chem. Soc.* 2017, ***139***, 1432–1435.
14 Lei, L.; Seyitliyev, D.; Stuard, S.; Mendes, J.; Dong, Q.; Fu, X.; Chen, Y.-A.; He, S.;Yi, X.; Zhu, L.; Chang, C.-H.; Ade, H.; Gundogdu, K.; So, F. Efficient Energy Funneling in Quasi-2D Perovskites: From Light Emission to Lasing. *Adv. Mater.* 2020, ***32***, 1906571.
15 Zhou, N.; Shen, Y.; Li, L.; Tan, S.; Liu, N.; Zheng, G.; Chen, Q.; Zhou, H. Exploration of Crystallization Kinetics in Quasi Two-Dimensional Perovskite and High Performance Solar Cells. *J. Am. Chem. Soc.* 2018, ***140***, 459–465.
16 Huang, Y.; Liu, T.; Li, D.; Zhao, D.; Amini, A.; Cheng, C.; Xing, G. Limitations and solutions for achieving high-performance perovskite tandem photovoltaics. *Nano Energy* 2021, ***88***, 106219.
17 Liang, X. et al. Promoting Energy Transfer Between Quasi-2D Perovskite Layers Toward Highly Efficient Red Light-Emitting Diodes. *Small* 2022, ***18***, 2204638.
18 Li, M.; Gao, Q.; Liu, P.; Liao, Q.; Zhang, H.; Yao, J.; Hu, W.; Wu, Y.; Fu, H. Amplified Spontaneous Emission Based on 2D Ruddlesden–Popper Perovskites. *Adv. Funct. Mater.* 2018, ***28***, 1707006.
19 Wagner, I.; Van Gompel, W. T.; Erkens, R.; Ruttens, B.; D'Haen, J.; Lutsen, L.; Vanderzande, D.; Chuang, C.; Chang, S. H.; Hume, P. A.; Price, M. B.; Geiregat, P.;Hodgkiss, J. M.; Chen, K. Critical Roles of Ultrafast Energy Funnelling and Ultrafast Singlet-Triplet Annihilation in Quasi-2D Perovskite Optical Gain Mechanisms. *Adv. Mater.* 2025, ***37***, 2419674.
20 Perez, C. M.; Ghosh, D.; Prezhdo, O.; Nie, W.; Tretiak, S.; Neukirch, A. Point Defects in Two-Dimensional Ruddlesden–Popper Perovskites Explored with Ab Initio Calculations. *J. Phys. Chem. Lett.* 2022, ***13***, 5213–5219.
21 Giulia, G.; Roldan-Carmona, C.; Zimmermann, I.; Mosconi, E.; Lee, X.; Martineau, D.; Narbey, S.; Oswald, F.; De Angelis, F.; Grätzel, M.; Nazeeruddin, M. K. One-Year Stable Perovskite Solar Cells by 2D/3D Interface Engineering. *Nat. Commun.* 2017, ***8***, 15684.
22 Selivanov, N. I.; Rozhkova, Y. A.; Kevorkyants, R.; Emeline, A. V.; Bahnemann, D. W. The effect of organic cations on the electronic, optical and luminescence properties of 1D piperidinium, pyridinium, and 3-hydroxypyridinium lead trihalides. *Dalton Trans.* 2020, ***49***, 4390–4403.
23 Kevorkyants, R.; Emeline, A.; Bahnemann, D. Hybrid lead triiodide perovskites with unsaturated heterocyclic cations containing N, O, and S atoms: Ab initio study. *Journal of Solid State Chemistry* 2020, ***282***, 121082.
24 Selivanov, N. I.; Murashkina, A. A.; Kevorkyants, R.; Emeline, A. V.; Bahnemann, D. W. Pyridinium lead tribromide and pyridinium lead triiodide: quasi-onedimensional perovskites with an optically active aromatic π-system. *Dalton Trans.* 2018, ***47***, 16313–16319.
25 Fu, W.; Zhao, T.; Liu, H.; Lin, F.; Zuo, L.; Li, X.; Jen, A. K.-Y. High-Efficiency Quasi2D Perovskite Solar Cells Incorporating 2,2'-Biimidazolium Cation. *Solar RRL* 2021, ***5***, 2000700.
26 Xu, H.; Hu, X.; Sun, F.; Sun, J.; Guo, W.; Liu, Y.; Liu, W.; Fu, X.; Luo, J.; Sun, Z. Visible-Photoactive Ferroelectric Semiconductor Incorporating Aromatic Dynamic Spacer Enables Optoelectronic Synaptic Plasticity. *Adv. Mater.* 2025, ***37,*** 2504953.
27 Zhou, Y.; Zhang, Y.; Zhang, L.; Wu, H.; Zhou, Y.; Xu, X.; Yu, J.; Wu, X.; Xie, J.; Fu, W.; Wu, G.; Chen, H. Aromatic Imidazole Diammonium-based 2D Dion-Jacobson Perovskites with Reduced Exciton Binding Energy. *Adv. Funct. Mater.* 2024, ***34***, 2408774.
28 Liu, Y.; Guo, J.; Zhou, H.; Li, C.; Guo, X. Correlating π-pi Stacking of Aromatic Diammoniums with Stability and Dimensional Reduction of Dion–Jacobson 2D Perovskites. *J. Am. Chem. Soc.* 2024, ***146***, 8198–8205.
29 Ebic, M.; Sadegh, F.; Ans, M.; Yadav, P.; Prochowicz, D.; Akin, S. Molecularly tailored quaternary pyridinium salt for post-treatment to enhance defect passivation and charge carrier dynamics in perovskite solar cells. *Journal of Energy Chemistry* 2025, ***109***, 120– 128.
30 Cha, J.; Beom Lee, C.; Min Park, S.; Baek, D.; Kim, S. Lattice-matched insitu-formed 1D perovskite phase in Multi-dimensional solar cells achieving high phase stability and favorable energy landscape. *Chemical Engineering Journal* 2024, ***484***, 149280.
31 Jiang., X.; Zhu, L.; Zhang, B.; Yang, G.; Zheng, L.; Dong, K.; Yin, Y.; Wang, M.; Liu, S.; Pang, S.; Guo, X. Insights Into the Role of π-Electrons of Aromatic Aldehydes in Passivating Perovskite Defects. *Angew. Chem. Int. Ed.* 2025, ***64***, e202420369.
32 Teale, S.; Degani, M.; Chen, B.; Sargent, E. H.; Grancini, G. Molecular cation and lowdimensional perovskite surface passivation in perovskite solar cells. *Nat. Energy* 2024, ***9***, 779–792.

Open Access Article. Published on 16 March 2026. Downloaded on 3/17/2026 4:36:31 AM.
This article is licensed under a Creative Commons Attribution-NonCommercial 3.0 Unported Licence.

Journal of Materials Chemistry A Accepted Manuscript

This journal is © The Royal Society of Chemistry 20xx

Please do not adjust margins

View Article Online
DOI: 10.1039/D6TA00037A

Open Access Article. Published on 16 March 2026. Downloaded on 3/17/2026 4:36:31 AM.
This article is licensed under a Creative Commons Attribution-NonCommercial 3.0 Unported Licence.

Journal of Materials Chemistry A Accepted Manuscript

33 Du, Y.; Wu, J.; Zhang, X.; Zhu, Q.; Zhang, M.; Liu, X.; Zou, Y.; Wang, S.; Sun, W. Surface passivation using pyridinium iodide for highly efficient planar perovskite solar cells. *J. Energy Chem.* 2021, ***52***, 84–91.

34 Li, B. et al. Harnessing strong aromatic conjugation in low-dimensional perovskite heterojunctions for high-performance photovoltaic devices. *Nat. Commun.* 2024, ***15***, 2753.

35 Maughan, A. E.; Kurzman, J. A.; Neilson, J. R. Hybrid Inorganic-Organic Materials with an Optoelectronically Active Aromatic Cation: $(C_7H_7)_2SnI_6$ and $C_7H_7PbI_3$. *Inorg. Chem.* 2015, ***54***, 370–378.

36 Oswald, I. W. H.; Mozur, E. M.; Moseley, I. P.; Ahn, H.; Neilson, J. R. Hybrid ChargeTransfer Semiconductors: $(C_7H_7)SbI_4$, $(C_7H_7)BiI_4$, and Their Halide Congeners. *Inorg. Chem.* 2019, ***58***, 5818–5826.

37 Shen, Y. et al. Strain regulation retards natural operation decay of perovskite solar cells. *Nature* 2024, *635*, 882–889.

38 Liu, Q.; Liang, W. Structure and property tunability in monolayer halide lead-free double hybrid perovskites: effects of Rashba and biaxial strain. *J. Mater. Chem. A* 2019, ***7*, 11487–11496.**

39 Lee, Y. B.; Cho, S. B.; Chung, Y. C. Tunable Indirect to Direct Bandgap Transition of Monolayer Sc_2CO_2 by the Strain Effect. *ACS Appl. Mater. Interfaces* 2014, ***140***, 14724–14728.

40 Sun, Y. J.; Wang, D.; Shuai, Z. G. Indirect-to-Direct Bandgap Crossover in Few-Layer Transition Metal Dichalcogenides: A Theoretical Prediction. *J. Phys. Chem. C* 2016, ***120***, 21866–21870.

41 Xu, W. P.; Zhao, J. Z.; Xu, H. Adsorption Induced Indirect-to-Direct Bandgap Transition in Monolayer Blue Phosphorus. *J. Phys. Chem. C* 2018, ***122***, 15792–15798.

42 Tu, Q.; Spanopoulos, I.; Hao, S.; Wolverton, C.; Kanatzidis, M. G.; Shekhawat, G. S.; Dravid, V. P. Probing Strain-Induced Bandgap Modulation in 2D Hybrid Organic–Inorganic Perovskites. *ACS Energy Letters* 2019, ***4***, 796–802.

43 Zi-Ang Nan, et al. Revealing phase evolution mechanism for stabilizing formamidinium-based lead halide perovskites by a key intermediate phase. *Chem* 2021, ***7***, 2513–2526.

44 Pilania, G.; Uberuaga, B. P. Cation ordering and effect of biaxial strain in double perovskite $CsRbCaZnCl_6$. *J. Appl. Phys.* 2015, ***117***, 114103.

45 Liu, D. et al. Strain relaxation in halide perovskites via 2D/3D perovskite heterojunction formation. *Sci. Adv.* 2025, ***11***, eadu3459.

46 Cheng, Q.; Wang, B.; Huang, G.; Li, Y.; Li, X.; Chen, J.; Yue, S.; Li, K.; Zhang, H.; Zhang, Y.; Zhou, H. Impact of Strain Relaxation on 2D Ruddlesden–Popper Perovskite Solar Cells. *Angew. Chem. Int. Ed.* 2022, ***61***, e202208264.

47 Li, Q.; Zheng, Y.; Wang, H.; Liu, X.; Lin, M.; Sui, X.; Leng, X.; Liu, D.; Wei, Z.; Song, M.; Li, D.; Yang, H. G.; Yang, S.; Hou, Y. Graphene-polymer reinforcement of perovskite lattices for durable solar cells. *Science* 2025, ***387***, 1069–1077.

48 Liu, Q.; Ju, M.-G.; Zeng, X. C. Unconventional perovskite-to-perovskite tandem cell designed by stacking with large-gap phosphonium-based analogs. *Materials Today Energy* 2024, ***42***, 101556.

49 Kresse, G. Ab-Initio Molecular-Dynamics for Liquid-Metals. *J. Non-Cryst. Solids* 1995, *193*, 222–229.

50 Blöchl, P. E. Projector Augmented-Wave Method. *Phys. Rev. B* 1994, ***50***, 17953–17979.

51 Perdew, J. P.; Burke, K.; Ernzerhof, M. Generalized Gradient Approximation Made Simple. *Phys. Rev. Lett.* 1996, ***77***, 3865–3868.

52 Grimme, S. Semiempirical GGA-type density functional constructed with a long-range dispersion correction. *J. Comp. Chem.* 2006, ***27***, 1787–99.

53 Grimme, S.; Antony, J.; Ehrlich, S.; Krieg, H. A consistent and accurate ab initio parametrization of density functional dispersion correction (DFT-D) for the 94 elements H-Pu. *J. Chem. Phys.* 2010, ***132***, 154104.

54 Moellmann, J.; Grimme, S. DFT-D3 Study of Some Molecular Crystals. *J. Phys. Chem. C* 2014, ***118***, 7615–7621.

55 Schleyer, P. v. R.; Maerker, A.; Dransfeld, A.; Jiao, H.; van Eikema Hommes, N. J. R. Nucleus-Independent Chemical Shifts: A Simple and Efficient Aromaticity Probe. *J. Am. Chem. Soc.* 1996, ***118***, 6317–6318.

56 Schleyer, P. v. R.; et al. Nucleus-Independent Chemical Shifts (NICS) as an Aromaticity Criterion. *Chem. Rev.* 2005, ***105***, 3842–3888.

57 Jiao, H.; et al. Aromaticity and Antiaromaticity in Five-Membered C_4H_4X Ring Systems. *Angew. Chem. Int. Ed.* 1997, ***36***, 976–978.

58 Neese, F. The SHARK Integral Generation and Digestion System. *J. Comp. Chem.* 2022, ***44***, 381.

59 Neese, F. The ORCA program system. *WIRES Comput. Molec. Sci.* 2012, ***2***, 73–78.

60 Neese, F. Software update: the ORCA program system, version 4.0. *WIRES Comput. Molec. Sci.* 2018, ***8***, 1–6.

61 Neese, F.; Wennmohs, F.; Becker, U.; Riplinger, C. The ORCA quantum chemistry program package. *J. Chem. Phys.* 2020, *152*, 224108.

62 Neese, F. Software update: The ORCA program system—Version 5.0. *WIRES Comput. Molec. Sci.* 2022, ***12***, e1606.

63 Neese, F. Approximate second-order SCF convergence for spin unrestricted wavefunctions. *Chem. Phys. Lett.* 2000, ***325***, 93–98.

64 Becke, A.D. Density-functional thermochemistry. III. The role of exact exchange, J. Chem. Phys., 1993, **98**, 5648.

65 Ditchfield, R. Self-consistent perturbation theory of diamagnetism. Mol. Phys., 1974, **27**, 789:.

66 Weigend, F. and Ahlrichs, R. Balanced basis sets of split valence, triple zeta valence and quadruple zeta valence quality for H to Rn: Design and assessment of second and third row. Phys. Chem. Chem. Phys., 2005, **7**, 3297.

67 Spitzer, W. G.; Fan, H. Y. Determination of Optical Constants and Carrier Effective Mass of Semiconductors. *Phys. Rev.* 1957, ***106***, 882–890.

68 Peksa, P.; Maufort, A.; Baranowski, M.; Surrente, A.; Lutsen, L.; Plochocka, P.; Van Gompel, W. T. M.; Dyksik, M. Engineering the Effective Mass in 2D Perovskites via Octahedral Distortion. *J. Phys. Chem. C* 2024, ***128***, 17984–17989.

69 Yu, W.; Zou, Y.; Wang, H.; Qi, S.; Wu, C.; Guo, X.; Liu, Y.; Chen, Z.; Qu, B.; Xiao, L. Breaking the bottleneck of lead-free perovskite solar cells through dimensionality modulation. *Chem. Soc. Rev.* 2024, ***53***, 1769–1788.

70 Ju, M. G.; Sun, G. X.; Zhao, Y.; Liang, W. Z. A Computational View of the Change in the Geometric and Electronic Properties of Perovskites Caused by the Partial Substitution of Pb by Sn. *Phys. Chem. Chem. Phys.* 2015, ***17***, 17679–17687.

71 Feng, J.; Xiao, B. Effective Masses and Electronic and Optical Properties of Nontoxic $MASnX_3$ (X = Cl, Br, and I) Perovskite Structures as Solar Cell Absorber: A Theoretical Study Using HSE06. *J. Phys. Chem. C* 2014, ***118***, 19655–19660.

72 Zhang, L.; Liang, W. Z. How the Structures and Properties of Two-Dimensional Layered Perovskites $MAPbI_3$ and $CsPbI_3$ Vary with the Number of Layers. *J. Phys. Chem. Lett.* 2017, ***8***, 1517–1523.

Please do not adjust margins

View Article Online
DOI: 10.1039/D6TA00037A

Data availability statement (RSC template)

The data supporting this article have been included as part of the Electronic Supplementary Information (ESI). Additional data that support the findings of this study are available from the corresponding author upon reasonable request.

Open Access Article. Published on 16 March 2026. Downloaded on 3/17/2026 4:36:31 AM.
This article is licensed under a Creative Commons Attribution-NonCommercial 3.0 Unported Licence.

Journal of Materials Chemistry A Accepted Manuscript